Nano Research

Open Access

Research Article

In-situ self-assemblied HTO/MXene/PSF hybrid membrane for high efficiency and selective lithium extraction from shale gas wastewater

Yuchun Ren[1], Dandan Zhao[1] ✉, Fei Zhou[5], Chen Fu[4], Yongsheng Fu[1], Zhenglian Wu[1], Ying Luo[6], Feng Sun[7], Xun He[3], and Xuping Sun[2,3] ✉

[1] *School of Environmental Science and Engineering, Southwest Jiaotong University, Chengdu 611756, China*
[2] *College of Chemistry, Chemical Engineering and Materials Science, Shandong Normal University, Jinan 250014, China*
[3] *Center for High Altitude Medicine, West China Hospital, Sichuan University, Chengdu 610041, China*
[4] *Chengdu Pollution Source Monitoring Center, Chengdu 610066, China*
[5] *Leshan Environmental Monitoring Center Station of Sichuan Province, Department of Ecology and Environment of Sichuan Province, Leshan 614000, China*
[6] *State Key Laboratory of Space Power Sources, Shanghai Institute of Space Power Sources, Shanghai 200245, China*
[7] *School of Materials Science and Engineering, Shanghai Jiao Tong University, Shanghai 200240, China*

Cite this article: *Nano Research*, **2025**, *18*, 94907261. https://doi.org/10.26599/NR.2025.94907261

ABSTRACT: H_2TiO_3 (HTO) emerges as a highly promising lithium-ion sieve (LIS) material for selectively and efficiently extracting lithium from liquid-phase systems. However, the practical use of conventional powdered HTO adsorbents is hindered by difficulties in recovery and titanium leaching, which limits their reusability. Herein, we design a novel HTO/MXene/polysulfone (HTO/MXene/PSF) hybrid membrane, where two-dimensional (2D) MXene nanosheets bridge PSF and HTO via enhanced hydrogen bonding and enable the *in-situ* self-assembly of HTO into spindle-like nanostructures. As anticipated, the hybrid membrane exhibits selective lithium adsorption, achieving a capacity of 25.80 mg·g^{-1} from shale gas wastewater (SGW). Moreover, it maintains remarkable cyclic stability with a negligible decrease in adsorption capacity of merely 0.25% after ten consecutive adsorption–desorption cycles. Besides, filtration studies demonstrate that a membrane with a surface area of 12.56 cm² can effectively process 230 mL of SGW. Theoretical calculations reveal that hydrogen bonding and electronic interactions drive the self-assembly of HTO on MXene and further elucidate the adsorption strength and spatial hindrance mechanisms for selective lithium ion adsorption. This study introduces an innovative concept of *in-situ* self-assembled LIS in a hybrid membrane for lithium recovery from SGW, which is expected to inspire further research on self-assembled sieve-based adsorbents.

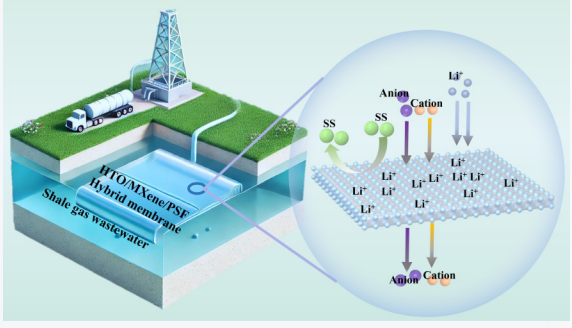

KEYWORDS: lithium recovery, shale gas wastewater, self-assembled lithium-ion sieve, H_2TiO_3/MXene hybrid membrane, density functional theory

1 Introduction

Lithium is an indispensable resource for the transition to renewable energy, primarily due to its extensive application in rechargeable batteries and the increasing prevalence of electric vehicles [1–3]. With demand for lithium expected to soon outpace supply, it is emerging as a resource of considerable geopolitical significance [4]. Currently, lithium is primarily sourced from brine deposits, seawater, and lithium-bearing ores [5]. Although recovery from these natural sources is increasingly well-understood, growing attention is being directed toward uncovering industrial waste lithium sources for environmental protection. Shale gas wastewater (SGW) has recently gained attention as an alternative resource for lithium recovery; however, the current technologies for lithium recovery from SGW, also known as shale gas flowback and produced water, remain underdeveloped [6]. SGW, particularly in the Sichuan Basin of China, contains significant lithium resources with an average concentration of 33.0 mg·L^{-1}. By 2030, the global volume of SGW is projected to range from 499 to 3585 million m^3, highlighting its considerable potential for lithium recovery [7, 8].

Received: November 24, 2024; **Revised:** December 30, 2024
Accepted: January 13, 2025

✉Address correspondence to Dandan Zhao, zhaodandan@swjtu.edu.cn; Xuping Sun, xpsun@uestc.edu.cn

Hitherto, chemical precipitation, solvent extraction, and electrochemical techniques are employed for lithium recovery from liquids [9–12]. Chemical precipitation typically necessitates large volumes of freshwater as an eluent, which may not be viable over the long term depending on regional availability. Similarly, solvent extraction generates considerable quantities of residual organic solvents and ionic liquids, raising significant environmental challenges. While electrochemical methods are considered eco-friendly, they face challenges related to high energy consumption and increased lithium recovery costs in large-scale applications. These issues limit their industrial viability. Notably, adsorption methods present several advantages, including low cost, reduced environmental impact, and ease of operation [13, 14]. Such attributes render adsorption an ideal approach for efficiently recovering lithium from SGW.

Currently, aluminum-based layered double hydroxide adsorbents (Li/Al-LDHs), manganese-based lithium ion-sieve adsorbents, and titanium-based lithium ion-sieve are employed for lithium recovery from aqueous sources [15–22]. Li/Al-LDHs exhibit low adsorption capacity and stability [23]. Manganese-based lithium ion-sieve adsorbents exhibit higher adsorption capacities, but their industrial application is hindered due to the significant manganese dissolution issues [24]. Among the titanium-based lithium ion-sieve adsrobents, H_2TiO_3 (HTO) [25, 26] and $H_4Ti_5O_{12}$ stand out, particularly H_2TiO_3, which is characterized by a stable crystal structure, excellent adsorption/desorption performance, and cycle durability, making it a preferred choice for lithium recovery from SGW [22, 25, 26].

Despite the advantages of titanium-based lithium ion-sieve adsorbents, its tendency to aggregate at the nanoscale necessitates further optimization through nanostructuring [27]. Fortunately, integrating titanium-based lithium ion-sieve adsorbents with mixed matrix membranes (MMMs) proves to be the optimal strategy for lithium recovery, as it combines the high adsorption capacity of titanium-based lithium ion-sieve adsorbents with the structural integrity of the membrane [28, 29]. Although MMMs hold significant potential in advanced separation processes, their practical application is often impeded by several challenges. Key issues include the poor dispersion of active particles within the polymer matrix, interfacial incompatibility between inorganic fillers and the polymer phase, and inferior long-term operational stability. MMMs rely on the physical dispersion of inorganic particles within a polymer matrix, which frequently lacks solid chemical bonds between components. In contrast, hybrid membranes form structures with stronger interactions, such as van der Waals force and hydrogen bonding, between fillers and the polymer matrix, leading to enhanced synergistic effects and improved performance [30–33]. Polysulfone (PSF) membranes, renowned for their chemical stability, mechanical strength, and tunable pore sizes, are particularly well-suited for such applications [34, 35]. MXenes with their layered structure and abundant surface functional groups (–OH, –O, –F), reduce ion diffusion barriers and facilitate multiple hydrogen bonding interactions, providing numerous nucleation sites [36–42]. The immobilization of MXene on PSF as a substrate for *in-situ* HTO growth offers a promising strategy to mitigate HTO agglomeration and enhance interfacial compatibility between HTO and the PSF. Such advancements are expected to significantly advance the selective lithium recovery from SGW.

Inspired by this, we developed a rapid *in-situ* self-assembly method to assemble HTO on MXene/PSF, resulting in the formation of spindle-shaped nanostructures and the generation of an adsorptive HTO/MXene/PSF hybrid membrane. In this process, MXene serves as a bridge between HTO and PSF through sequential hydrogen bonding, facilitating the ordered self-assembly of HTO onto the MXene template and anchoring it to the PSF membrane. Using SGW, we conducted a combined experimental and computational study on the adsorption capacity, kinetics, selectivity, and regenerability of the HTO/MXene/PSF hybrid membrane. The filtration efficiency of the membrane was assessed through dynamic filtration studies. The self-assembly of HTO on the membrane surface presents a novel approach to preparing a hybrid membrane. The HTO/MXene/PSF hybrid membrane avoids additional filtration, prevents secondary pollution, and simplifies recovery, making it a candidate for lithium extraction from SGW or other liquids.

2 Experimental

2.1 Materials

The SGW used in our experiments was sourced from a shale gas well located in Luxian County, Luzhou City, Sichuan Province, China. We procured nitric acid (HNO_3), hydrofluoric acid (HF), hydrogen peroxide (H_2O_2), tetrabutylammonium hydroxide (TBAOH), hydrochloric acid (HCl), and sodium hydroxide (NaOH) from Chengdu Kelong Chemical Reagent Co., Ltd. Titanium dioxide (TiO_2), lithium chloride (LiCl), ethanol (EtOH), lithium hydroxide (LiOH) and N-methyl pyrrolidone (NMP) were supplied by Aladdin Co., Ltd. Ti_3AlC_2 was sourced from Shandong Xiyan New Material Technology Co., Ltd. PSF (Solvay-P-3500) was obtained from Wuxi Titan Chemical Corporation.

2.2 Sample preparation procedure

2.2.1 *Synthesis of MXene in NMP*

The preparation process of $Ti_3C_2T_x$ (MXene) has been documented in a previous study [43]. Specifically, 3 g of Ti_3AlC_2 was etched using 30 mL of 40% HF with continuous stirring at room temperature for 24 h. After etching, the mixture was centrifuged and washed with deionized water until a neutral pH was achieved. The precipitate was collected and vacuum-dried at 60 °C for 12 h to obtain multilayer MXene. Subsequently, 2 g of the multilayer MXene was added to 30 mL of 15 wt.% TBAOH and stirred at room temperature for 6 h. The mixture was then centrifuged and washed once with EtOH, followed by the addition of NMP to collect the precipitate by centrifugation. The precipitate was redispersed in 150 mL of NMP and sonicated for 30 min, after which the upper black solution was collected.

2.2.2 *Synthesis of Li_2TiO_3*

According to the literature, Li_2TiO_3 (LTO) was synthesized using a hydrothermal method [29]. In a typical experimental procedure, A mixture containing 3.990 g of TiO_2 and 2.395 g of LiOH was prepared using deionized water as the solvent and then transferred to a Teflon-lined autoclave. The solution was subjected to hydrothermal conditions at 160 °C for 24 h. Afterward, the resultant mixture was filtered to isolate the white precipitate, which was subsequently subjected to thermal treatment in a tube furnace at 500 °C for 2 h. The final product, obtained after cooling, was designated as LTO.

2.2.3 *Synthesis of HTO/MXene/PSF hybrid membrane*

A solution containing 16 wt.% PSF in 84 wt.% MXene-dispersed

NMP was prepared at 50 °C. LTO was added and stirred at room temperature to achieve a homogeneous mixture for membrane casting. Various LTO proportions were used to optimize performance (Table S1 in the Electronic Supplementary Material (ESM)). The solution was cast onto glass using a 200 μm casting knife without non-woven support. Following this, the cast solution was immersed in deionized water to form an LTO/MXene/PSF hybrid membrane. This membrane was then converted to an HTO/MXene/PSF hybrid membrane by immersing it in 0.2 M HCl for 24 h. After acid treatment, the membrane was rinsed with ultra-pure water and dried for use.

2.3 Characterization

X-ray diffraction (XRD) analysis was conducted using a SHIMADZU Cu Kα radiation source (40 kV, 30 mA). Scanning electron microscopy (SEM) was performed at 5 kV with ZEISS equipment. High-resolution field emission transmission electron microscopy (HRTEM, FEI Talos f200x) was used to characterize the MXene. X-ray photoelectron spectroscopy (XPS) using a Thermo ESCALAB 250XI analyzed the composition of the HTO/MXene/PSF hybrid membrane. Fourier-transform infrared (FT-IR) spectra were obtained with an Agilent 1260. Surface morphology and roughness of PSF, MXene/PSF and HTO/MXene/PSF hybrid membrane were analyzed for atomic force microscopy (AFM) using Bruker Multimode 8. Membrane surface areas were measured using Brunauer–Emmett–Teller (BET) analysis on a QUADRASORB SI instrument in N_2. Contact angles were measured with a KRÜSS ADVANCE goniometer. Tensile strength tests were conducted using a UTM5305H instrument. The concentrations of ions were analyzed using inductively coupled plasma optical emission spectrometry (ICP-OES) Optima 8000 model. Inductively coupled plasma mass spectrometry (ICP-MS) analysis was performed on NexION 1000G.

2.4 Batch adsorption experiments

Details of the adsorption and filtration experiments are provided in the ESM.

3 Results and discussion

3.1 Characterization of HTO/MXene/PSF hybrid membrane

The schematic illustration of LIS nanostructure assembly on MXene nanosheets is shown in Fig. 1(a). Ti_3AlC_2 is etched into multilayer MXene and uniformly dispersed in NMP via ultrasonication. MXene nanosheets inherently possess surface functional groups such as –OH and –F, which confer good solubility in water and NMP, facilitating electrostatic and hydrogen bonding interactions [44]. PSF in NMP forms hydrogen bonding with MXene, after which LTO is introduced. LTO converts into HTO upon HCl acid treatment. During the acid treatment, HTO nanoparticles also self-assemble on MXene nanosheets through hydrogen bonding and electronic interaction, forming spindle-like nanostructures that reduce surface energy. The HTO assembly on two-dimensional materials is spontaneous, driven by free energy reduction, and occurs under ambient conditions without external intervention. In contrast to hydrothermal synthesis, this self-assembly process effectively mitigates the oxidation of MXene nanosheets in aqueous solutions induced by dissolved oxygen.

As determined by SEM, the unetched Ti_3AlC_2 powder presents distinct, well-defined layered aggregates, which is the characteristic feature of the MAX phase structure (Fig. 1(b)). Owing to the selective removal of Al atoms during the etching process, the resulting MXene sheets exhibit a smooth, two-dimensional nanosheet morphology with notable uniformity in thickness, lateral dimensions, and elemental distribution (Figs. 1(c)–1(f)). The TEM image of MXene sheets (Fig. 1(g)) reveals lattice fringes with a spacing of 0.25 nm, corresponding to the (006) plane of the $Ti_3C_2T_x$ phase (Figs. 1(h) and 1(i)). Figure 1(j) further confirms the homogeneous distribution of F, O, Ti, and C elements on the monodisperse MXene surface, with N originating from NMP.

Figure 2(a) illustrates the SEM image of the pristine PSF membrane, revealing a relatively low porosity on the membrane surface. After the introduction of MXene nanosheets and LTO nanoparticles presented in Fig. S1 in the ESM, the resulting membrane exhibited a notably roughened surface (Figs. 2(b) and 2(c)). Subsequent hydrogen exchange in HCl prompted the self-assembly of negatively charged HTO onto the positively charged MXene surface, facilitated by electronic interactions and hydrogen bonding, culminating in the formation of a spindle-like nanostructure (Figs. 2(d) and 2(e)). The PSF membrane (Fig. S2 in the ESM) seems white, while the MXene/PSF membrane (Fig. S3 in the ESM) is black, indicating a uniform MXene dispersion. Similarly, the LTO/MXene/PSF membrane (Fig. S4 in the ESM) appears gray and uniform. A cross-sectional image of the HTO/MXene/PSF hybrid membrane (Fig. 2(f)) reveals a macro-void or sponge-like porous morphology. Compared to the pristine PSF and MXene/PSF membrane (Figs. S5 and S6 in the ESM) and pre-hydrogen exchange state (Fig. S7 in the ESM), the cross-sectional morphology appears denser. The SEM and corresponding energy-dispersive X-ray spectroscopy (EDX) elemental mapping (Figs. 2(g) and 2(h), and Fig. S8 in the ESM) confirm the uniformity of the membrane. Moreover, EDX analysis (Fig. S9 in the ESM) on HTO/MXene/PSF hybrid membrane validates the consistent dispersion of elements, namely C, O, F, Ti, Cl and S.

AFM analysis revealed the impact of HTO and MXene incorporation on membrane surface roughness. The pristine PSF membrane (Figs. 3(a) and 3(b)) had an average roughness (R_a) of 7.91 nm, consistent with previously reported PSF membranes [45]. Incorporating MXene (Figs. 3(c) and 3(d)) increased the R_a to 13.36 nm, while further incorporation of HTO (Figs. 3(e) and 3(f)) raised it to 33.90 nm. The addition of nanoparticles alters surface texture, affecting morphology and permeability. This stems from delayed inverse transition due to increased casting solution viscosity, boosting surface density. Additionally, *in-situ* self-assembly of HTO on MXene surfaces during hydrogen exchange forms nanostructures, increasing membrane roughness. Research shows that rougher membranes have a larger surface area, affecting both adsorption capacity and water flux [46, 47]. Substrate morphology is crucial, and rough surfaces enhance adhesion between the ion sieve and substrate. The nitrogen adsorption–desorption isotherms in Figs. 3(g)–3(j), following the classification by the International Union of Pure and Applied Chemistry (IUPAC), exhibit a typical type IV isotherm with an H_3 hysteresis loop [48]. The pattern suggests the presence of mesopores within the adsorbent. Adsorption assessment involved testing pristine PSF, MXene/PSF, and HTO/MXene/PSF hybrid membrane for BET surface area, pore volume, and average pore size (Table S3 in the ESM). MXene/PSF blending showed minimal change (Figs. 3(g) and 3(h)).

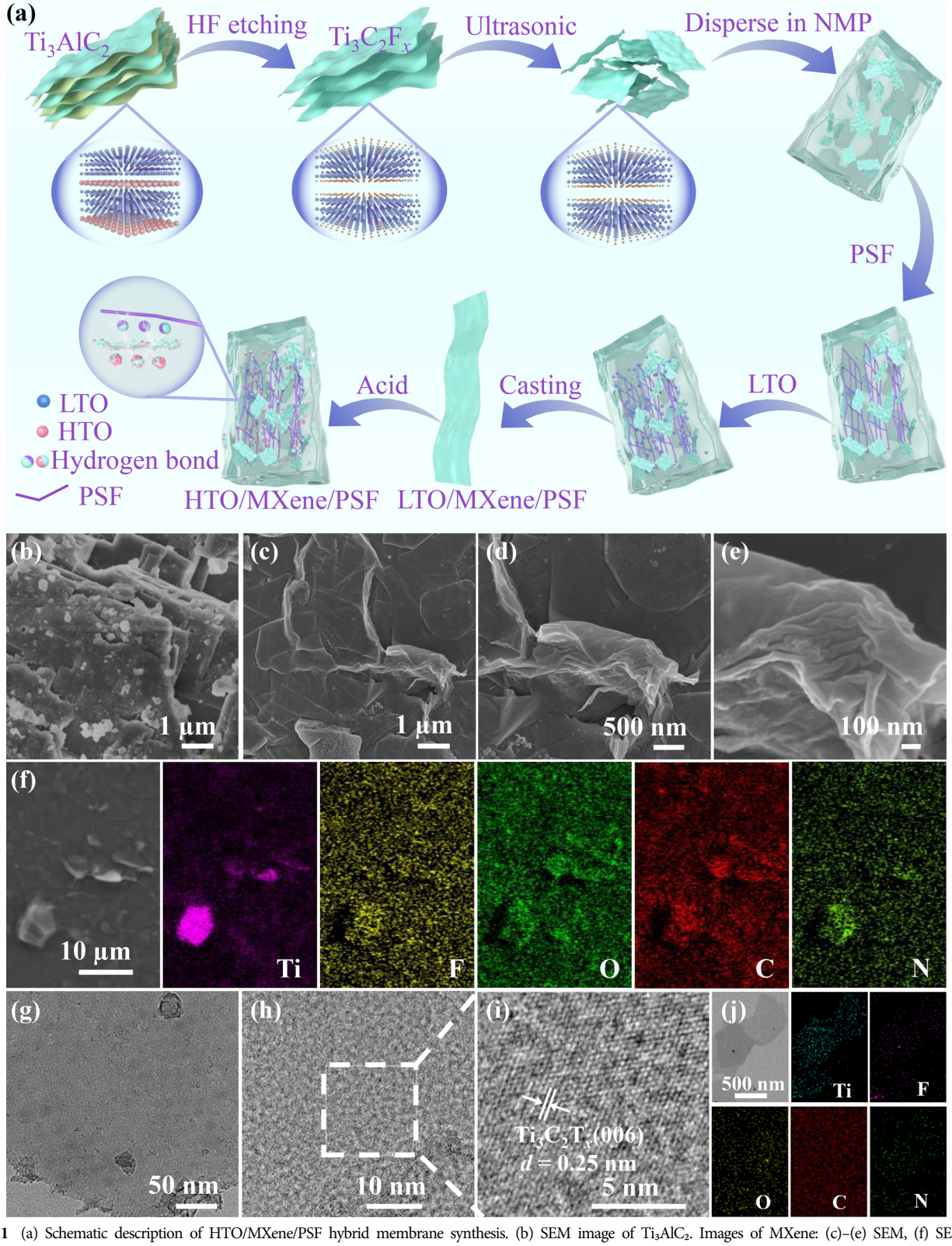

Figure 1 (a) Schematic description of HTO/MXene/PSF hybrid membrane synthesis. (b) SEM image of Ti_3AlC_2. Images of MXene: (c)–(e) SEM, (f) SEM and corresponding elemental mapping, (g) TEM, (h) and (i) HRTEM, and (j) TEM and corresponding elemental mapping.

The pristine PSF membrane had a surface area of 17.67 $m^2 \cdot g^{-1}$, while the HTO/MXene/PSF hybrid membrane increased to 38.44 $m^2 \cdot g^{-1}$. HTO addition increased HTO/MXene/PSF hybrid membrane surface area, primarily via *in-situ* self-assembly, expanding specific surface area for more adsorption sites. BJH pore size analysis (insets of Figs. 3(i) and 3(j)) revealed typical mesoporous structures with sizes mainly between 2 and 50 nm. After adsorption, the BET surface area of the HTO/MXene/PSF hybrid membrane decreased with a smaller pore size due to lithium ion occupancy.

Figure 4(a) demonstrates that blending PSF with MXene reduces

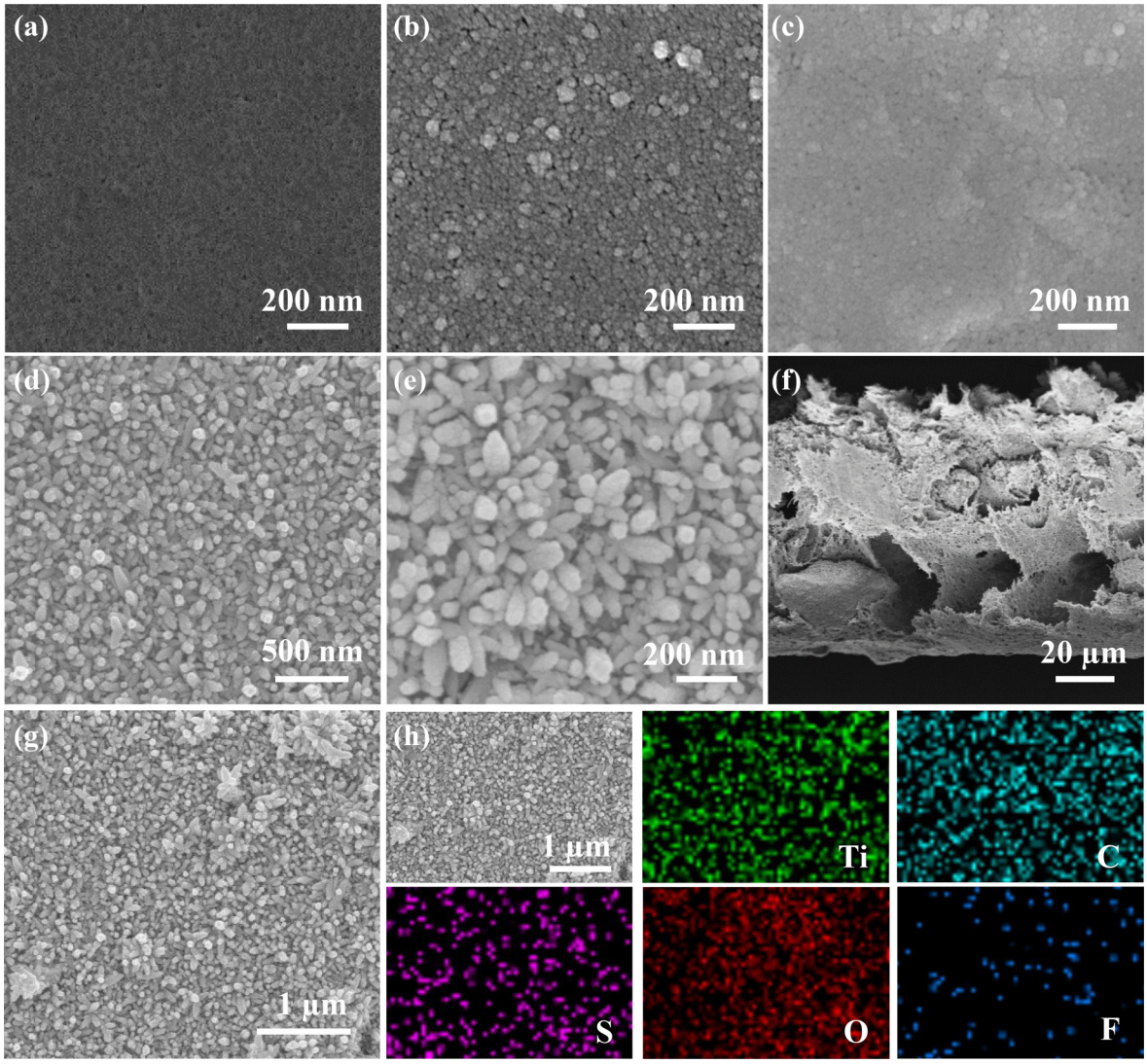

Figure 2 SEM images of (a) PSF, (b) MXene/PSF, (c) LTO/MXene/PSF membrane, and (d) and (e) HTO/MXene/PSF hybrid membrane. (f) Cross-sectional SEM image of HTO/MXene/PSF hybrid membrane. (g) and (h) SEM and corresponding EDX elemental mapping images of HTO/MXene/PSF hybrid membrane surface.

the contact angle from 81.24° to 75.59°. Notably, the contact angle of the HTO/MXene/PSF hybrid membrane increased to 83.50°, reflecting enhanced surface hydrophobicity. HTO self-assembles on MXene to form spindle-shaped nanostructures. The surface roughness of the membrane is significantly increased, the actual contact area between water droplets and the membrane surface is reduced, and the air is trapped within the spindle-shaped nanostructures, further enhancing the hydrophobicity of the membrane. The heightened surface roughness enhances solid-liquid contact and boosts apparent surface area [49]. Figure 4(b) shows XRD spectra before and after acid treatment. LTO pattern consistent with Li_2TiO_3 (PDF #00-033-0831). After acid treatment, although LTO patterns exhibit minimal change, slight shifts in peaks towards higher 2-theta values are noted, which are attributed to the Li^+-H^+ exchange reaction. The stress–strain curve of the membrane was obtained at ambient temperature, as depicted in Fig. 4(c). Both the maximum tensile stress and strain of the HTO/MXene/PSF hybrid membrane are lower than those of the MXene/PSF membrane and the PSF membrane. In the FTIR spectra of Fig. 4(d), the stretching vibration peaks of O=S=O at 1168 and 1235 cm^{-1} have weakened after blending with MXene and LIS, compared to pure PSF. Additionally, the emergence of a minor Ti–O peak at 670 cm^{-1} confirms the successful self-assembly of HTO on MXene/PSF. The formation of the hybrid membrane induces the attenuation of low-wavenumber fingerprint peaks in PSF.

Density functional theory (DFT) calculations were carried out to investigate the interfacial interactions in the HTO/MXene/PSF hybrid membrane. Figures 4(e)–4(g) present charge density differences and electron localization function (ELF) maps for three interfaces: MXene-MXene, MXene-PSF, and MXene-HTO, arranged by increasing charge transfer (Q). The iso-surface was set with a value of 0.003 e·$Å^{-3}$. The results show that adsorption strength increases with higher Q values, following this order: MXene-MXene (weak hydrogen bonding) < MXene-PSF (hydrogen bonding) < MXene-HTO (strong hydrogen bonding). The ELF maps confirm this trend, showing minimal electron localization for MXene-MXene interactions and significant localization for MXene-HTO, indicative of stronger interfacial bonding. Figure S10 in the ESM shows the opposite surface potentials of MXene and HTO, with MXene positively charged and HTO negatively charged. The enhanced adsorption strength and

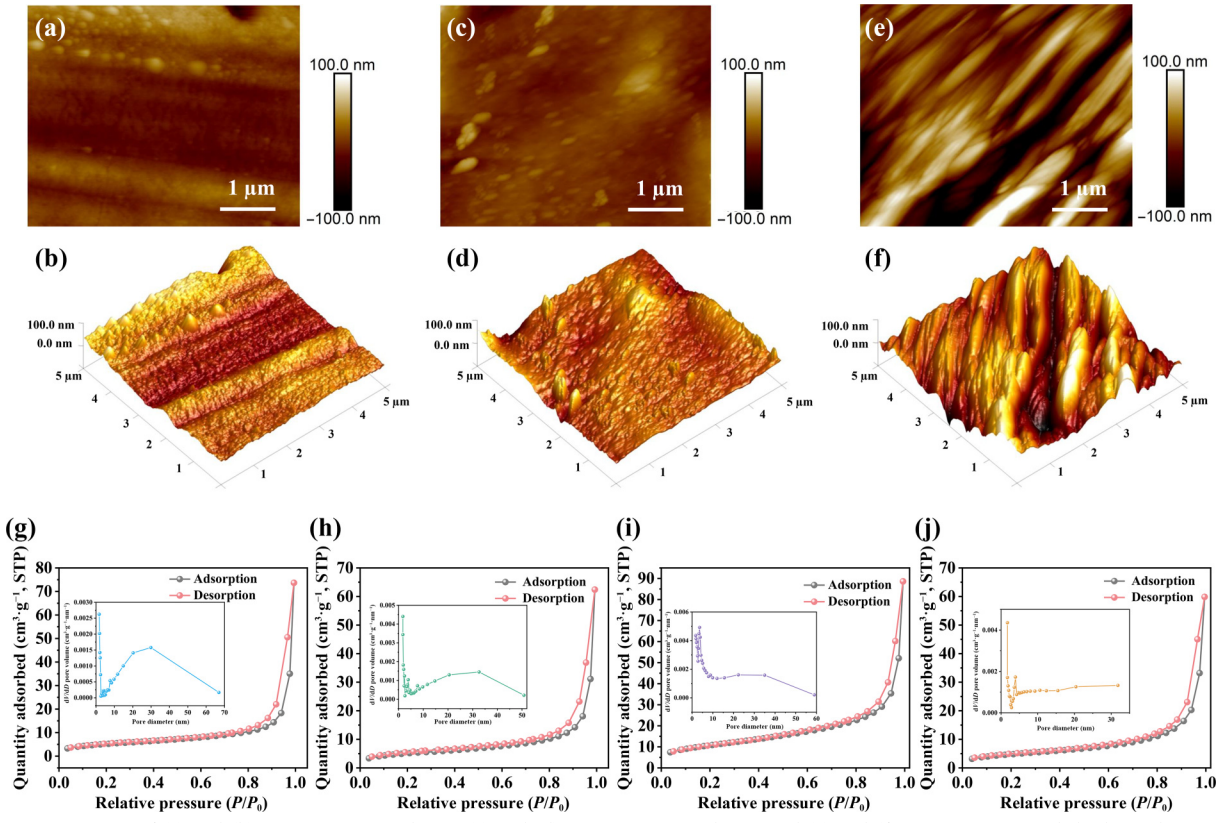

Figure 3 AFM images of (a) and (b) pristine PSF membrane, (c) and (d) MXene/PSF membrane, and (e) and (f) HTO/MXene/PSF hybrid membrane. BET N_2 adsorption–desorption isotherms (inset: pore size distribution) for (g) PSF membrane, (h) MXene/PSF membrane, (i) HTO/MXene/PSF hybrid membrane before adsorption of lithium ion, and (j) HTO/MXene/PSF hybrid membrane after adsorption of lithium ion.

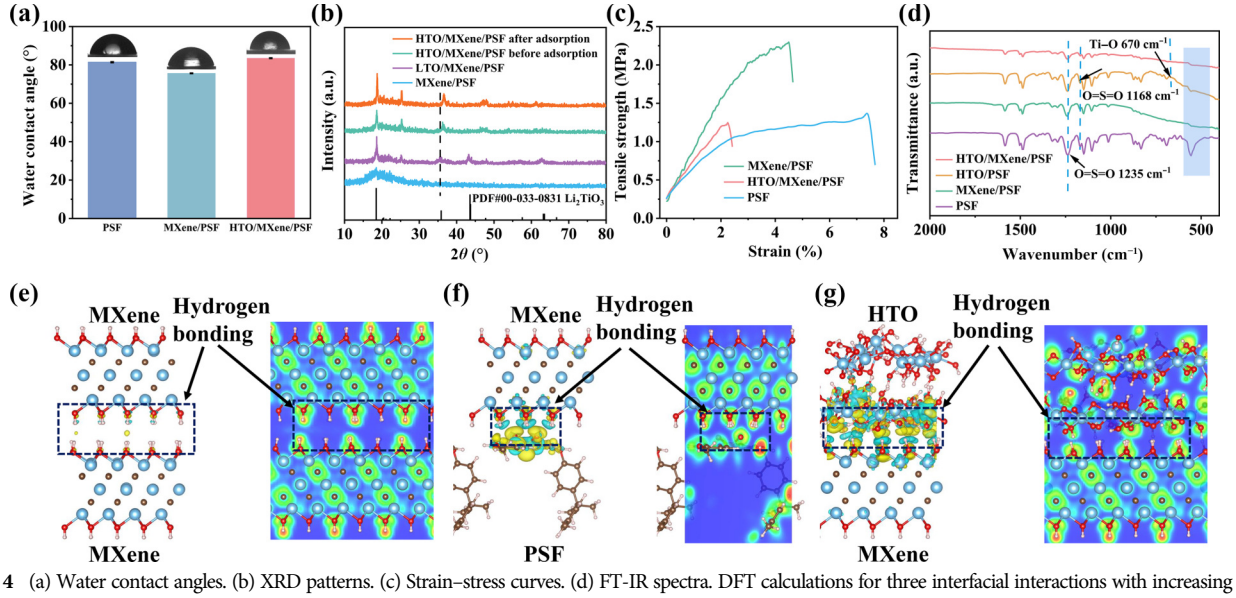

Figure 4 (a) Water contact angles. (b) XRD patterns. (c) Strain–stress curves. (d) FT-IR spectra. DFT calculations for three interfacial interactions with increasing Q: (e) MXene-MXene (weak hydrogen bonding), (f) MXene-PSF (hydrogen bonding), and (g) MXene-HTO (strong hydrogen bonding).

different electronic properties drive HTO self-assembly onto MXene.

3.2 Lithium adsorption performance

3.2.1 Influence of pH

To determine the best HCl concentration for lithium extraction, we treated the LTO/MXene/PSF membrane with varying acid concentrations. Figure 5(a) shows that lithium extraction remained stable from 0.2 to 0.5 M HCl. However, above 0.2 M, titanium leaching notably increased (Fig. S11 in the ESM). Therefore, 0.2 M HCl was chosen for further study, maximizing lithium extraction while minimizing titanium leaching from LTO. The adsorption capacity of the HTO/MXene/PSF hybrid membrane for lithium ion is significantly influenced by pH levels. As illustrated in Fig. 5(b), the adsorption capacity increases with rising pH, reaching

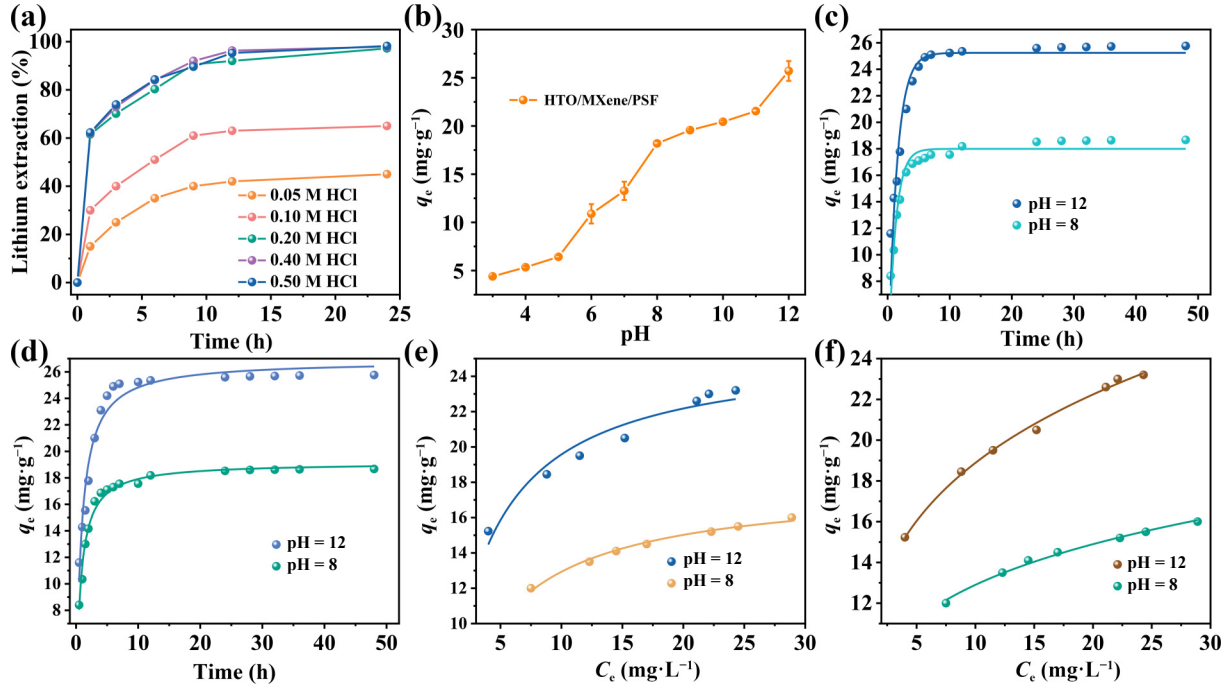

Figure 5 (a) Lithium extraction from HTO/MXene/PSF hybrid membrane at different HCl concentrations. (b) Effect of different pH levels for SGW. Adsorption kinetics in SGW: (c) pseudo-first-order and (d) pseudo-second-order equations. Adsorption isotherms with (e) Langmuir and (f) Freundlich models.

25.80 mg·g^{-1} at pH 12. Under alkaline conditions, abundant OH^- facilitates H^+-Li^+ exchange, enhancing lithium ion adsorption on the HTO/MXene/PSF hybrid membrane [50, 51]. The elevation in OH^- concentration facilitates the expulsion of H^+ from the lattice and facilitates the migration of Li^+, consequently enhancing the adsorption capacity. Hence, an alkaline solution is more advantageous for the adsorption of Li^+ by HTO [52]. Notably, in natural SGW (pH 8), the adsorption capacity of the HTO/MXene/PSF hybrid membrane reaches 18.19 mg·g^{-1}, rendering this condition favorable for engineering applications.

3.2.2 *Adsorption kinetics*

The lithium adsorption kinetics on HTO/MXene/PSF hybrid membranes were investigated under two different pH conditions (Figs. 5(c) and 5(d)). In SGW, lithium exhibited rapid adsorption within the initial 12 h, subsequently showing a significant decrease in adsorption rate until equilibrium was reached around 24 h. The kinetic parameters, as shown in Table S4 in the ESM, confirmed that the adsorption process of lithium ion on the adsorbents followed a pseudo-second-order kinetic model, revealing that chemical adsorption predominantly governed the adsorption rate [53]. Particularly noteworthy was the expedited attainment of maximum adsorption capacity at pH 12, surpassing the equilibrium time observed at natural SGW (pH 8), consistent with the Li^+-H^+ exchange process. The *in situ* self-assembly of HTO on the MXene surface generates spindle-like nanostructures, thereby augmenting the specific surface area and exposing more adsorption sites. Experimental adsorption capacities (pH 8, Li-SGW: 18.19 mg·g^{-1}; pH 12, Li-SGW: 25.80 mg·g^{-1}) closely aligned with those calculated based on the pseudo-second-order kinetic model (pH 8, Li-SGW: 19.14 mg·g^{-1}; pH 12, Li-SGW: 26.85 mg·g^{-1}). Kinetic experiments also conducted at two pure LiCl concentrations (Figs. S12(a) and S12(b) in the ESM) confirmed the membrane's applicability, with the maximum concentration tested being 100 mg·L^{-1}. The adsorption capacity (27.29 mg·L^{-1}) was comparable to that achieved in SGW, indicating that the hybrid membrane is well-suited for lithium recovery from SGW.

3.2.3 *Adsorption isotherms*

Figures 5(e) and 5(f) and Fig. S13 in the ESM depict the fitting results of the adsorption isotherms in SGW and LiCl, with the corresponding adsorption isotherm parameters listed in Table S5 in the ESM. At an adsorbent dosage of 0.5 g·L^{-1}, adsorption equilibrium was achieved when the lithium ion concentration in the LiCl solution reached 100 mg·L^{-1}, further defining the effective concentration range for adsorption. The findings indicate that the Freundlich model exhibits a more robust correlation compared to the Langmuir model, suggesting that lithium adsorption on HTO/MXene/PSF hybrid membrane primarily occurs in a multilayer adsorption form. The Langmuir model assumes uniform surface adsorption, while the Freundlich model describes heterogeneous surface adsorption with varying adsorption energies at different sites [54]. Additionally, the self-assembly of HTO enhances surface heterogeneity in the membrane, leading to variable adsorption energies at different sites, which may result in varying affinities for lithium ion.

3.2.4 *Reusability*

The variation in lithium adsorption capacity during the recovery process is crucial for evaluating the efficacy of the adsorbent. Consideration of structural stability and outstanding reusability is also essential for reducing the cost of the adsorption process. The regeneration performance of the HTO/MXene/PSF hybrid membrane was evaluated through ten adsorption and desorption cycles. Lithium ion adsorbed was removed through acid washing and subsequent adsorption cycles, as depicted in Figs. S14(a) and S14(b) in the ESM. Due to self-assembly structural stability, the lithium ion adsorption capacity in SGW remained relatively stable after each regeneration, with only slight declines observed. As shown in Figs. S14(c) and 14(d) in the ESM, all cycles resulted in

the complete desorption of lithium ion through acid washing, facilitating the reuse of the adsorption membrane. Furthermore, negligible titanium leaching occurred during each cycle. The demonstrated potential of HTO/MXene/PSF hybrid membrane for repeated use in SGW underscores the promising prospect of lithium resource recovery from SGW.

3.2.5 *Filtration study*

Figure S15 in the ESM demonstrates the time-dependent variation in permeate flux, showing a gradual decrease until reaching a steady state. The water flux of the MXene/PSF membrane is notably low, at only 14 $L{\cdot}m^{-2}{\cdot}h^{-1}$. In contrast, upon *in-situ* self-assembly of HTO onto the MXene/PSF matrix, forming a novel nanostructure, the water flux experiences a considerable increase, reaching at least 104 $L{\cdot}m^{-2}{\cdot}h^{-1}$. Water flux increases with the addition of LTO (Fig. S16 in the ESM). A comprehensive evaluation of the HTO/MXene/PSF hybrid membrane should encompass continuous filtration studies, estimating the retention capability of the adsorption membrane through breakthrough curve analysis. As depicted in Figs. 6(a) and 6(b), filtration results of fresh and regenerated membranes were examined using SGW with an initial lithium ion concentration of 25.60 $mg{\cdot}L^{-1}$. It is noteworthy that at natural SGW (pH 8), the effluent concentration of lithium ion reached its maximum value when the filtrate volume reached 210 mL, indicating complete permeation of Li^+ through the membrane. Conversely, at pH 12, the effluent concentration peaked when the filtrate volume reached 230 mL, possibly due to the higher OH^- concentration favoring Li^+-H^+ exchange. The HTO/MXene/PSF hybrid membrane exhibits excellent reusability in filtration experiments, retaining stable adsorption efficiency and structural integrity after four cycles and subsequent regeneration. The morphology of membrane surface ion sieves during the experimental process remained largely unaffected (Fig. S17 in the ESM), validating the reusability of the HTO/MXene/PSF hybrid membrane. The filtration study results further demonstrate the efficacy of this system in lithium ion retention.

3.3 Adsorption mechanism

3.3.1 *Selectivity*

Investigating the selectivity of HTO/MXene/PSF hybrid membrane for lithium ion is essential due to the coexistence of various cations in SGW. As demonstrated in Fig. 7(a), HTO/MXene/PSF hybrid membrane consistently exhibits a higher distribution coefficient (K_d) for lithium ion at both natural SGW (pH 8) and pH 12. The K_d value for lithium ion surpasses that of other ions, indicating high selectivity for lithium ion adsorption (Tables S6 and S7 in the ESM). Moreover, there is a minimal concentration of magnesium ion in SGW, with magnesium ion precipitating before adsorption initiation at pH 12. At natural SGW (pH 8), with minimal competition from magnesium adsorption, the substantial advantage in lithium recovery from SGW becomes evident, presenting a promising avenue for novel lithium recovery sources. Additionally, we compared the HTO/MXene/PSF hybrid membrane prepared in this work for lithium recovery from SGW with other LIS reported in the literature for lithium recovery from other solutions, as summarized in Table S8 in the ESM.

3.3.2 *DFT studies*

DFT calculations show that HTO has higher adsorption energies for Ba^{2+}, Ca^{2+}, and Li^+ than for K^+, Na^+, and Mg^{2+}, as demonstrated in

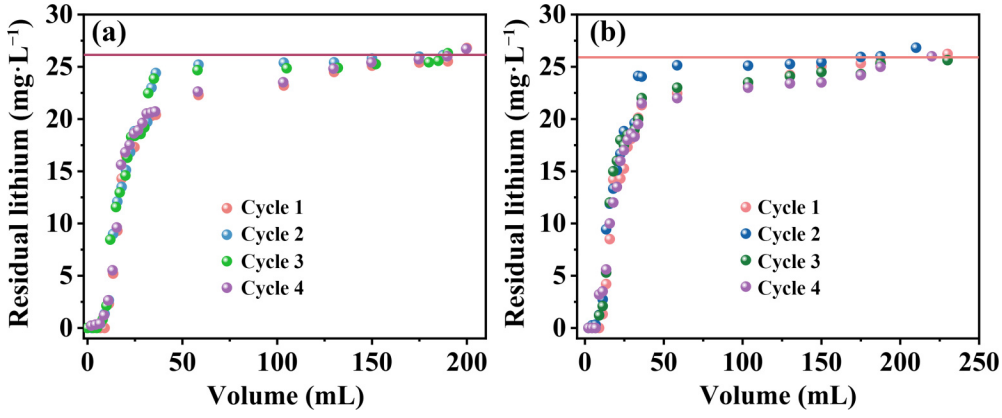

Figure 6 Filtration study of lithium ion by HTO/MXene/PSF hybrid membrane at (a) pH 12 and (b) natural (pH 8) in SGW (TMP = 0.035 MPa, T = 25 °C).

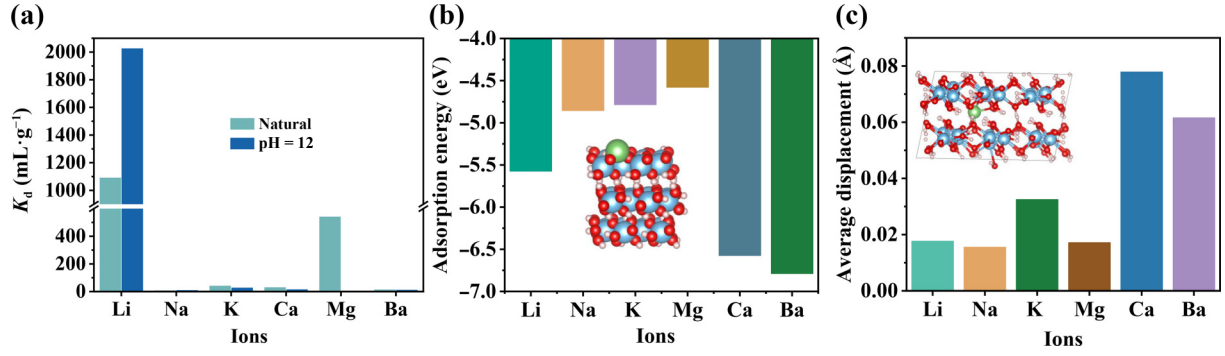

Figure 7 (a) Adsorption selectivity in SGW. (b) Adsorption energies of different metals on HTO. (c) Unit cell deformation induced by different ion insertions in the HTO lattice.

Figs. S18 and S19 in the ESM and Fig. 7(b), indicating stronger interactions with these ions. The insertion of various ions into different sites of the HTO crystal lattice (Fig. S20 in the ESM) induces significant variations in lattice distortion, with Ca^{2+} and Ba^{2+} causing the most pronounced effects. Figure 7(c) shows that Li^+ induces the least lattice distortion, maintaining material stability and promoting selective Li^+ adsorption. The strong adsorption energy and spatial hindrance accelerate Li^+ migration to active sites, ensuring high adsorption capacity and selectivity. As a result, the HTO/MXene/PSF hybrid membrane enables rapid adsorption and effective Li^+ separation due to the combined actions of MXene and HTO.

3.3.3 *XPS analysis*

Furthermore, XPS was utilized to investigate the surface electronic states and chemical compositions of the engineered HTO/MXene/PSF hybrid membrane before and after lithium ion adsorption. The XPS spectra (Fig. 8(a)) reveal distinct lithium peaks after adsorption, demonstrating the effective capture of lithium ion by the HTO/MXene/PSF hybrid membrane. The high-resolution XPS analysis of the Ti 2p region (Fig. 8(b)) displayed initial peaks at 458.76 and 464.46 eV, corresponding to the $2p_{3/2}$ and $2p_{1/2}$ orbits of Ti^{4+}, respectively [55–57]. Notably, a subtle shift of 0.10 eV in the Ti $2p_{3/2}$ peak was observed after lithium adsorption, suggesting the formation of Li–O–Ti bonds, indicative of the modification of the H–O–Ti bond [58]. Despite the shift Ti preserved its +4 oxidation state, suggesting the adsorption operates via ion exchange, not through a redox process. After adsorption, the Li 1s high-resolution spectrum (Fig. 8(c)) displayed a new peak at 54.48 eV, attributed to the newly formed Li–O bonds [59]. In contrast, the before adsorption state revealed no significant Li 1s peak, emphasizing effective lithium desorption during the acid leaching phase. Furthermore, the O 1s spectrum (Fig. 8(d)) was deconvoluted into several peaks at 530.21, 531.05, 532.19, 533.03, and 533.94 eV, representing various oxygen-containing functional groups (Ti–O, C=O, C–O–C, S=O, and C–OH) [60–64]. The peaks exhibited a shift in binding energies, indicative of the structural transformations prompted by lithium interaction. In Fig. 8(e), peaks in the S 2p spectrum are identified at 168.88 and 167.77 eV, which correspond to the S $2p_{1/2}$ and S $2p_{3/2}$ states, respectively [65, 66]. Figure 8(f) shows the C 1s spectrum with two prominent peaks at 286.30 and 284.64 eV, associated respectively with C–O and C–H/C–C bonds [67, 68].

4 Conclusions

In summary, we present the fabrication of an HTO/MXene/PSF hybrid membrane for selective lithium recovery from SGW. The membrane was synthesized through the *in-situ* self-assembly of HTO on MXene, resulting in a lithium adsorption capacity of 25.80 $mg \cdot g^{-1}$. With an active surface area of 12.56 cm^2, the membrane demonstrated effective lithium ion recovery from 230 mL of SGW. The selective adsorption of Li^+ over competing ions was driven by an H^+-Li^+ exchange mechanism, as confirmed by adsorption isotherms, kinetics studies, and XPS. DFT calculations indicate that interfacial electrostatic interactions and enhanced hydrogen bonding between MXene and HTO promote the *in-situ* assembly of HTO on MXene. Strong lithium adsorption energy and minimal distortion of the HTO crystal lattice with lithium intercalation demonstrate strong selectivity for lithium ion recovery. Consequently, this methodology holds promise for developing a lithium resource recovery process from SGW, ensuring a sustainable lithium supply for future energy needs.

Electronic Supplementary Material: Supplementary material (SEM images, surface electrostatic potential, cycle stability, membrane flux, DFT models, and Tables S1–S8) is available in the online version of this article at https://doi.org/10.26599/NR.2025.94907261.

Data availability

All data needed to support the conclusions in the paper are presented in the manuscript and the Electronic Supplementary Material. Additional data related to this paper may be requested from the corresponding author upon request.

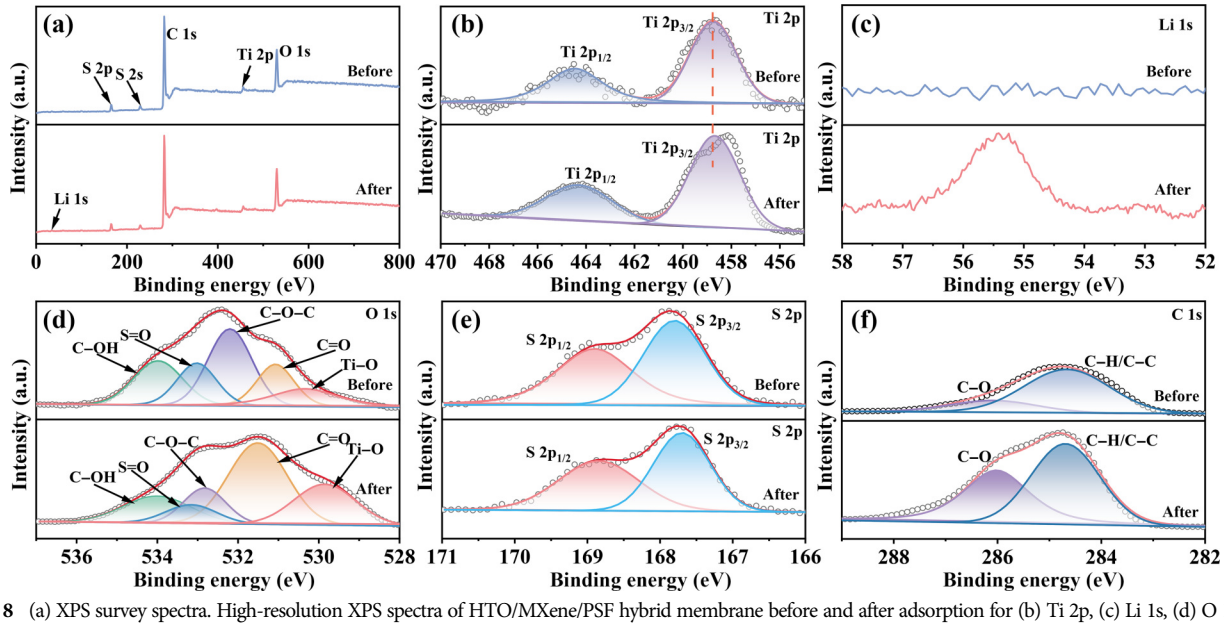

Figure 8 (a) XPS survey spectra. High-resolution XPS spectra of HTO/MXene/PSF hybrid membrane before and after adsorption for (b) Ti 2p, (c) Li 1s, (d) O 1s, (e) S 2p, and (f) C 1s.

Acknowledgements

This work was supported by the Fundamental Research Funds for the Central Universities (No. 2682024CX106), Yangtze River Ecological Environment Protection and Restoration (No. 2022-LHYJ-02-0509-09), and the Industry-University-Research Cooperation Fund of Shanghai Academy of Spaceflight Technology (No. USCAST2021-21).

Declaration of competing interest

All the contributing authors report no conflict of interests in this work.

Author contribution statement

Y. C. R.: Writing manuscript, experimental design, data curation. D. D. Z.: Project administration, validation, writing manuscript. F. Z.: Data curation, writing manuscript. C. F.: Data curation, validation. Y. S. F.: Funding acquisition, validation. Z. L. W.: Data curation. Y. L.: Data curation. F. S.: Data curation. X. H.: Data curation. X. P. S.: Project administration, validation, experimental design.

Use of AI statement

None.

References

[1] Castelvecchi, D. Electric cars and batteries: How will the world produce enough. *Nature* **2021**, *596*, 336–339.

[2] Lu, Q. C.; Liu, P.; Zhou, T. Y.; Huang, R. L.; Zhang, K. X.; Hu, L.; Liu, R.; Ren, Z. B.; Wang, J. Y.; Wang, X. L. Recent progress on electro-sorption technology for lithium recovery from aqueous sources. *Nano Res.* **2024**, *17*, 2563–2573.

[3] Olivetti, E. A.; Ceder, G.; Gaustad, G. G.; Fu, X. K. Lithium-ion battery supply chain considerations: Analysis of potential bottlenecks in critical metals. *Joule* **2017**, *1*, 229–243.

[4] Razmjou, A.; Asadnia, M.; Hosseini, E.; Habibnejad Korayem, A.; Chen, V. Design principles of ion selective nanostructured membranes for the extraction of lithium ions. *Nat. Commun.* **2019**, *10*, 5793.

[5] Song, Y.; Fang, S. Q.; Xu, N.; Wang, M. N.; Chen, S. Y.; Chen, J.; Mi, B. X.; Zhu, J. Solar transpiration-powered lithium extraction and storage. *Science* **2024**, *385*, 1444–1449.

[6] Kumar, A.; Fukuda, H.; Hatton, T. A.; Lienhard, J. H. Lithium recovery from oil and gas produced water: A need for a growing energy industry. *ACS Energy Lett.* **2019**, *4*, 1471–1474.

[7] Tian, L.; Liu, Y. H.; Tang, P.; Yang, Y. S.; Wang, X. R.; Chen, T. X.; Bai, Y. H.; Tiraferri, A.; Liu, B. C. Lithium extraction from shale gas flowback and produced water using $H_{1.33}Mn_{1.67}O_4$ adsorbent. *Resour., Conserv., Recycl.*, **2022**, *185*, 106476.

[8] Xie, W. C.; Tian, L.; Tang, P.; Cui, J. Y.; Wang, T. J.; Zhu, Y. M.; Bai, Y. H.; Tiraferri, A.; Crittenden, J. C.; Liu, B. C. Shale gas wastewater characterization: Comprehensive detection, evaluation of valuable metals, and environmental risks of heavy metals and radionuclides. *Water Res.* **2022**, *220*, 118703.

[9] Haddad, A. Z.; Hackl, L.; Akuzum, B.; Pohlman, G.; Magnan, J. F.; Kostecki, R. How to make lithium extraction cleaner, faster and cheaper-in six steps. *Nature* **2023**, *616*, 245–248.

[10] Bai, X.; Dai, J. D.; Ma, Y.; Bian, W. B.; Pan, J. M. 2-(Allyloxy) methylol-12-crown-4 ether functionalized polymer brushes from porous PolyHIPE using UV-initiated surface polymerization for recognition and recovery of lithium. *Chem. Eng. J.* **2020**, *380*, 122386.

[11] Xu, P.; Hong, J.; Qian, X. M.; Xu, Z. W.; Xia, H.; Tao, X. C.; Xu, Z. Z.; Ni, Q. Q. Materials for lithium recovery from salt lake brine. *J. Mater. Sci* **2021**, *56*, 16–63.

[12] Li, Z.; Chen, I. C.; Cao, L.; Liu, X. W.; Huang, K. W.; Lai, Z. P. Lithium extraction from brine through a decoupled and membrane-free electrochemical cell design. *Science* **2024**, *385*, 1438–1444.

[13] Sun, J.; Li, X. W.; Huang, Y. H.; Luo, G. L.; Tao, D. J.; Yu, J. T.; Chen, L. L.; Chao, Y. H.; Zhu, W. S. Preparation of high hydrophilic H_2TiO_3 ion sieve for lithium recovery from liquid lithium resources. *Chem. Eng. J.* **2023**, *453*, 139485.

[14] Khalil, A.; Mohammed, S.; Hashaikeh, R.; Hilal, N. Lithium recovery from brine: Recent developments and challenges. *Desalination* **2022**, *528*, 115611.

[15] Zhong, J.; Lin, S.; Yu, J. G. Effects of excessive lithium deintercalation on Li^+ adsorption performance and structural stability of lithium/aluminum layered double hydroxides. *J. Colloid Interface Sci.* **2020**, *572*, 107–113.

[16] Zhang, L. J.; Zhang, T. T.; Zhao, Y. L.; Dong, G. F.; Lv, S. K.; Ma, S. L.; Song, S. X.; Quintana, M. Doping engineering of lithium-aluminum layered double hydroxides for high-efficiency lithium extraction from salt lake brines. *Nano Res.* **2024**, *17*, 1646–1654.

[17] Paranthaman, M. P.; Li, L.; Luo, J. Q.; Hoke, T.; Ucar, H.; Moyer, B. A.; Harrison, S. Recovery of lithium from geothermal brine with lithium-aluminum layered double hydroxide chloride sorbents. *Environ. Sci. Technol.* **2017**, *51*, 13481–13486.

[18] Zhang, G. T.; Hai, C. X.; Zhou, Y.; Tang, W. P.; Zhang, J. Z.; Zeng, J. B.; Liu, Y. H.; Dong, S. D.; Peng, G. P. Al and F ions co-modified $Li_{1.6}Mn_{1.6}O_4$ with obviously enhanced Li^+ adsorption performances. *Chem. Eng. J.* **2022**, *450*, 137912.

[19] Ding, K. Y.; Zhu, G. R.; Song, C. H.; Wang, Q.; Wang, L.; Wang, Z. Q.; Meng, C. X.; Gao, C. J. Fabrication of polyacrylonitrile-$Li_{1.6}Mn_{1.6}O_4$ composite nanofiber flat-sheet membranes via electrospinning method as effective adsorbents for Li^+ recovery from salt-lake brine. *Sep. Purif. Technol.* **2022**, *284*, 120242.

[20] Li, X. W.; Chao, Y. H.; Chen, L. L.; Chen, W.; Luo, J.; Wang, C.; Wu, P. W.; Li, H. M.; Zhu, W. S. Taming wettability of lithium ion sieve via different TiO_2 precursors for effective Li recovery from aqueous lithium resources. *Chem. Eng. J.* **2020**, *392*, 123731.

[21] Li, X. W.; Chen, L. L.; Chao, Y. H.; Zhu, L. H.; Luo, G. L.; Sun, J.; Jiang, L.; Zhu, W. S.; Liu, Z. C.; Xu, C. M. Highly selective separation of lithium with hierarchical porous lithium-ion sieve microsphere derived from MXene. *Desalination* **2022**, *537*, 115847.

[22] Zhao, B.; Qiao, Y. J.; Qian, Z. Q.; Wei, W. F.; Li, J.; Wu, Z. J.; Liu, Z. Unraveling the Li^+ desorption behavior and mechanism of $Li_4Ti_5O_{12}$ with different facets to enhance lithium extraction. *J. Mater. Chem. A* **2023**, *11*, 7094–7104.

[23] Zhong, J.; Lin, S.; Yu, J. G. Li^+ adsorption performance and mechanism using lithium/aluminum layered double hydroxides in low grade brines. *Desalination* **2021**, *505*, 114983.

[24] Qian, F. R.; Zhao, B.; Guo, M.; Wu, Z. J.; Zhou, W. Z.; Liu, Z. Surface trace doping of Na enhancing structure stability and adsorption properties of $Li_{1.6}Mn_{1.6}O_4$ for Li^+ recovery. *Sep. Purif. Technol* **2021**, *256*, 117583.

[25] Zhang, L. Y.; Zhou, D. L.; Yao, Q. Q.; Zhou, J. B. Preparation of H_2TiO_3-lithium adsorbent by the sol–gel process and its adsorption performance. *Appl. Surf. Sci.* **2016**, *368*, 82–87.

[26] Zhao, K. Y.; Li, J.; Yuan, J. Y.; Yu, X. P.; Guo, Y. F.; Jiang, Z. Z.; Li, M. L.; Duo, J.; Deng, T. L. A novel Co-doped H_2TiO_3 spinning composite for efficient lithium recovery from alkaline lithium precipitation mother liquor. *Chem. Eng. J.* **2024**, *482*, 148989.

[27] Zhang, L. J.; Zhang, T. T.; Lv, S. K.; Song, S. X.; Galván, H. J. O.;

Quintana, M.; Zhao, Y. L. Adsorbents for lithium extraction from salt lake brine with high magnesium/lithium ratio: From structure-performance relationship to industrial applications. *Desalination* **2024**, *579*, 117480.

[28] Miao, J.; Zhao, K. Y.; Guo, F.; Xu, L. N.; Xie, Y. C.; Deng, T. L. Novel LIS-doped mixed matrix membrane absorbent with high structural stability for sustainable lithium recovery from geothermal water. *Desalination* **2022**, *527*, 115570.

[29] Lin, H. Y.; Yu, X. P.; Li, M. L.; Duo, J.; Guo, Y. F.; Deng, T. L. Synthesis of polyporous ion-sieve and its application for selective recovery of lithium from geothermal water. *ACS Appl. Mater. Interfaces* **2019**, *11*, 26364–26372.

[30] Cheng, X. X.; Pan, F. S.; Wang, M. R.; Li, W. D.; Song, Y. M.; Liu, G. H.; Yang, H.; Gao, B. X.; Wu, H.; Jiang, Z. Y. Hybrid membranes for pervaporation separations. *J. Memb. Sci.* **2017**, *541*, 329–346.

[31] Zhang, B.; Dai, X. Y.; Wei, N. N.; Cui, X. C.; Fan, F. Q.; Zhang, J. D.; Zhang, D. L.; Meng, F. B.; Qi, W.; Fu, Y. Fabrication of oriented MOF-based mixed matrix membrane via ion-induced synchronous synthesis. *Small* **2024**, *20*, 2305688.

[32] Yu, L. T.; Hao, L. Q.; Feng, Y.; Pang, J.; Guo, M. W.; Li, L. J.; Fan, W. D.; Fan, L. L.; Wang, R. M.; Kang, Z. X. et al. Assembling ionic liquid into porous molecular filler of mixed matrix membrane to trigger high gas permeability, selectivity, and stability for CO_2/CH_4 separation. *Nano Res.* **2024**, *17*, 4535–4543.

[33] Goh, S. H.; Lau, H. S.; Yong, W. F. Metal-organic frameworks (MOFs)-based mixed matrix membranes (MMMs) for gas separation: A review on advanced materials in harsh environmental applications. *Small* **2022**, *18*, 2107536.

[34] Yang, P. F.; Xu, L. L.; Trogadas, P.; Coppens, M. O.; Lan, Y. Bioinspired supramolecular macrocycle hybrid membranes with enhanced proton conductivity. *Nano Res.* **2024**, *17*, 797–805.

[35] Miller, D. J.; Dreyer, D. R.; Bielawski, C. W.; Paul, D. R.; Freeman, B. D. Surface modification of water purification membranes. *Angew. Chem., Int. Ed.* **2017**, *56*, 4662–4711.

[36] Zhang, N. N.; Huang, S.; Yuan, Z. S.; Zhu, J. C.; Zhao, Z. F.; Niu, Z. Q. Direct self-assembly of MXene on Zn anodes for dendrite-free aqueous zinc-ion batteries. *Angew. Chem., Int. Ed.* **2021**, *60*, 2861–2865.

[37] Wei, C. L.; Tao, Y.; An, Y. L.; Tian, Y.; Zhang, Y. C.; Feng, J. K.; Qian, Y. T. Recent advances of emerging 2D MXene for stable and dendrite-free metal anodes. *Adv. Funct. Mater.* **2020**, *30*, 2004613.

[38] Kang, Y.; Hu, T.; Wang, Y. Q.; He, K. Q.; Wang, Z. Y.; Hora, Y.; Zhao, W.; Xu, R. M.; Chen, Y.; Xie, Z. L. et al. Nanoconfinement enabled non-covalently decorated MXene membranes for ion-sieving. *Nat. Commun.* **2023**, *14*, 4075.

[39] Cao, W. T.; Chen, F. F.; Zhu, Y. J.; Zhang, Y. G.; Jiang, Y. Y.; Ma, M. G.; Chen, F. Binary strengthening and toughening of MXene/cellulose nanofiber composite paper with nacre-inspired structure and superior electromagnetic interference shielding properties. *ACS Nano* **2018**, *12*, 4583–4593.

[40] Wan, S. J.; Li, X.; Chen, Y.; Liu, N. N.; Du, Y.; Dou, S. X.; Jiang, L.; Cheng, Q. F. High-strength scalable MXene films through bridging-induced densification. *Science* **2021**, *374*, 96–99.

[41] Li, W.; Zhou, T. Z.; Zhang, Z. J.; Li, L.; Lian, W. W.; Wang, Y. L.; Lu, J. F.; Yan, J.; Wang, H. G.; Wei, L. et al. Ultrastrong MXene film induced by sequential bridging with liquid metal. *Science* **2024**, *385*, 62–68.

[42] Yang, J.; Li, M. Z.; Fang, S. L.; Wang, Y. L.; He, H. Y.; Wang, C. L.; Zhang, Z. J.; Yuan, B. C.; Jiang, L.; Baughman, R. H. et al. Water-induced strong isotropic MXene-bridged graphene sheets for electrochemical energy storage. *Science* **2024**, *383*, 771–777.

[43] Zhang, Q. X.; Lai, H. R.; Fan, R. Z.; Ji, P. Y.; Fu, X. L.; Li, H. High concentration of $Ti_3C_2T_x$ MXene in organic solvent. *ACS Nano.* **2021**, *15*, 5249–5262.

[44] Liu, Y. T.; Zhang, P.; Sun, N.; Anasori, B.; Zhu, Q. Z.; Liu, H.; Gogotsi, Y.; Xu, B. Self-assembly of transition metal oxide nanostructures on MXene nanosheets for fast and stable lithium storage. *Adv. Mater.* **2018**, *30*, 1707334.

[45] Mu, Y. F.; Feng, H.; Zhang, S. L.; Zhang, C. Y.; Lu, N.; Luan, J. S.; Wang, G. B. Development of highly permeable and antifouling ultrafiltration membranes based on the synergistic effect of carboxylated polysulfone and bio-inspired co-deposition modified hydroxyapatite nanotubes. *J. Colloid Interface Sci.* **2020**, *572*, 48–61.

[46] Rana, D.; Matsuura, T. Surface modifications for antifouling membranes. *Chem. Rev.* **2010**, *110*, 2448–2471.

[47] Ho, C. D.; Chang, H.; Chang, C. L.; Huang, C. H. Theoretical and experimental studies of flux enhancement with roughened surface in direct contact membrane distillation desalination. *J. Memb. Sci.* **2013**, *433*, 160–166.

[48] Sing, K. S. W. Reporting physisorption data for gas/solid systems with special reference to the determination of surface area and porosity (Recommendations 1984). *Pure Appl. Chem.* **1985**, *57*, 603–619.

[49] Wenzel, R. N. Resistance of solid surfaces to wetting by water. *Ind. Eng. Chem.* **1936**, *28*, 988–994.

[50] Wang, Q. H.; Yang, X. Y.; Li, C. W.; Zhao, C. Y.; Huang, Y. J.; Qiu, S. Q.; Qin, Y. R.; Shi, C. L. Titanium-based lithium ion sieve adsorbent H_2TiO_3 with enhanced Li^+ adsorption properties by magnetic Fe doping. *Sep. Purif. Technol* **2024**, *346*, 127455.

[51] Qu, W.; Fu, Y. C.; Zhang, Y. S.; Wang, W. C.; Xu, C.; Liu, C.; Zhang, Y.; Wang, Q.; Liu, B. C. Structural/surficial dual regulated granular H_2TiO_3 lithium-ion sieves for lithium extraction from salt lake brine. *J. Clean. Prod.* **2024**, *449*, 141789.

[52] Liu, Q.; Xing, H. F.; Zhang, Y.; Zhao, Y. Z.; Rong, M.; Liu, H. Z.; Yang, L. R. Highly hydrophilic H_2TiO_3 ion sieve with neodymium (Nd) doping enables fast and high-efficiency Li extraction. *Sep. Purif. Technol.* **2024**, *345*, 127263.

[53] Song, Y. C.; Tan, H. H.; Qin, S. L.; Liu, Z.; Liu, C. T.; Shen, C. Y.; Yang, P. P.; Li, S. W. Assembly of a core-shell MOF with stability into polyacrylamide hydrogel for boosting extraction of uranium from seawater. *Nano Res.* **2024**, *17*, 3398–3406.

[54] Nassar, N. N.; Hassan, A.; Pereira-Almao, P. Effect of surface acidity and basicity of aluminas on asphaltene adsorption and oxidation. *J. Colloid Interface Sci.* **2011**, *360*, 233–238.

[55] Cai, Z. W.; Zhao, D. L.; Fan, X. Y.; Zhang, L. C.; Liang, J.; Li, Z. X.; Li, J.; Luo, Y. S.; Zheng, D. D.; Wang, Y. et al. Rational construction of heterostructured $Cu_3P@TiO_2$ nanoarray for high-efficiency electrochemical nitrite reduction to ammonia. *Small* **2023**, *19*, 2300620.

[56] Deng, Z. Q.; Li, L.; Ren, Y. C.; Ma, C. Q.; Liang, J.; Dong, K.; Liu, Q.; Luo, Y. L.; Li, T. S.; Tang, B. et al. Highly efficient two-electron electroreduction of oxygen into hydrogen peroxide over Cu-doped TiO_2. *Nano Res.* **2022**, *15*, 3880–3885.

[57] Wu, T. W.; Zhu, X. J.; Xing, Z.; Mou, S. Y.; Li, C. B.; Qiao, Y. X.; Liu, Q.; Luo, Y. L.; Shi, X. F.; Zhang, Y. N. et al. Greatly improving electrochemical N_2 reduction over TiO_2 nanoparticles by iron doping. *Angew. Chem., Int. Ed.* **2019**, *58*, 18449–18453.

[58] Wei, S. D.; Wei, Y. F.; Chen, T.; Liu, C. B.; Tang, Y. H. Porous lithium ion sieves nanofibers: General synthesis strategy and highly selective recovery of lithium from brine water. *Chem. Eng. J.* **2020**, *379*, 122407.

[59] Li, C. B.; Yu, J. L.; Yang, L.; Zhao, J. X.; Kong, W. H.; Wang, T.; Asiri, A. M.; Li, Q.; Sun, X. P. Spinel $LiMn_2O_4$ nanofiber: An efficient electrocatalyst for N_2 reduction to NH_3 under ambient conditions. *Inorg. Chem.* **2019**, *58*, 9597–9601.

[60] Li, L.; Chen, H. J.; Li, L.; Li, B. H.; Wu, Q. B.; Cui, C. H.; Deng, B.; Luo, Y. L.; Liu, Q.; Li, T. S. et al. La-doped TiO_2 nanorods toward boosted electrocatalytic N_2-to-NH_3 conversion at ambient conditions. *Chin. J. Catal.* **2021**, *42*, 1755–1762.

[61] Yu, Y.; Yu, L.; Wang, C. H.; Chen, J. P. An innovative yttrium nanoparticles/PVA modified PSF membrane aiming at

decontamination of arsenate. *J. Colloid Interface Sci.* **2018**, *530*, 658–666.

[62] Wang, L. W.; Fang, F.; Liu, Y.; Li, J.; Huang, X. J. Facile preparation of heparinized polysulfone membrane assisted by polydopamine/polyethyleneimine co-deposition for simultaneous LDL selectivity and biocompatibility. *Appl. Surf. Sci.* **2016**, *385*, 308–317.

[63] Casetta, J.; Ortiz, D. G.; Pochat-Bohatier, C.; Bechelany, M.; Miele, P. Atomic layer deposition of TiO_2 on porous polysulfone hollow fibers membranes for water treatment. *Sep. Purif. Technol.* **2023**, *312*, 123377.

[64] He, J. S.; Song, Y. H.; Chen, J. P. Development of a novel biochar/PSF mixed matrix membrane and study of key parameters in treatment of copper and lead contaminated water. *Chemosphere* **2017**, *186*, 1033–1045.

[65] Yue, L. C.; Wu, D. H.; Wu, Z. G.; Zhao, W. X.; Wang, D.; Zhong, B. H.; Liu, Q.; Liu, Y.; Gao, S. Y.; Asiri, A. M. et al. A MnS/FeS_2 heterostructure with a high degree of lattice matching anchored into carbon skeleton for ultra-stable sodium-ion storage. *J. Mater. Chem. A* **2021**, *9*, 24024–24035.

[66] Xia, L.; Wu, X. F.; Wang, Y.; Niu, Z. G.; Liu, Q.; Li, T. S.; Shi, X. F.; Asiri, A. M.; Sun, X. P. S-doped carbon nanospheres: An efficient electrocatalyst toward artificial N_2 fixation to NH_3. *Small Methods* **2019**, *3*, 1800251.

[67] Shi, Q.; Ni, L.; Zhang, Y. F.; Feng, X. S.; Chang, Q. H.; Meng, J. Q. Poly(p-phenylene terephthamide) embedded in a polysulfone as the substrate for improving compaction resistance and adhesion of a thin film composite polyamide membrane. *J. Mater. Chem. A* **2017**, *5*, 13610–13624.

[68] Liang, J.; Liu, P. Y.; Li, Q. Y.; Li, T. S.; Yue, L. C.; Luo, Y. S.; Liu, Q.; Li, N.; Tang, B.; Alshehri, A. A. et al. Amorphous boron carbide on titanium dioxide nanobelt arrays for high-efficiency electrocatalytic NO reduction to NH_3. *Angew. Chem., Int. Ed.* **2022**, *61*, e202202087.